AAS 23-100

REDUCED-ORDER MODEL FOR SPACECRAFT SWARM ORBIT DESIGN

Shane Lowe[*] **Simone D'Amico**[†]

This paper presents a reduced-order model for use in the design of relative orbits for spacecraft swarm missions. Spacecraft swarms provide significant advantages compared to traditional, monolithic spacecraft, including improved robustness to failure owing to the distribution of payload tasks and the ability to create large, time-varying baselines between individual spacecraft. These advantages come at the cost of increased mission complexity, requiring mission designers to consider collision avoidance, the relative orbits of spacecraft within the swarm, as well as the maintenance and reconfiguration of the swarm. The problem of spacecraft swarm orbit design has been addressed in the literature for specific orbital scenarios, and many of its associated challenges have also been investigated, either in isolation or as members of various subsets. However, existing methods have significant limitations which make them unsuited to the more general problem of spacecraft swarm orbit design. A reduced-order model is proposed to enable swarm orbit design. It is based on a parameterization of the spacecraft relative motion in terms of relative orbital elements, which permits the straightforward visualization of relative orbit geometry, the analytical inclusion of perturbations and maneuvers, as well as the analytical computation of minimum inter-spacecraft separation distances over extended time periods. The utility of the reduced-order model is demonstrated in several scenarios which are representative of the challenges facing the Space Weather Atmospheric Reconfigurable Multiscale Experiment (SWARM-EX), an upcoming spacecraft swarm mission. Performance of the reduced-order model is then validated through comparison with high-fidelity numerical simulation.

INTRODUCTION

Building on the success of early missions such as GRACE, PRISMA, and TanDEM-X, spacecraft formation flying and the broader field of distributed space systems (DSS) are rapidly entering into the mainstream of space mission design.[1–3] The advantages offered by DSS, including improved robustness to failure owing to the distribution of payload tasks among spacecraft, and the ability to create large, time-varying baselines between individual spacecraft, are attractive to mission designers seeking to accomplish groundbreaking mission objectives. A new generation of missions utilizing distributed architectures, including the Starling Formation-Flying Optical Experiment (StarFOX), the Virtual Super Optics Reconfigurable Swarm (VISORS), Cal X-1, and the Space Weather Atmospheric Reconfigurable Multiscale Experiment (SWARM-EX), will push the boundaries of distributed optical navigation, heliophysics, X-ray astronomy, and aeronomy, respectively.[4–7] The use of distributed architectures that enable these exciting advances comes at the cost of substantially increased mission complexity. The challenges of mission design for traditional, monolithic spacecraft are already considerable. However, this problem is taken to an extreme when employing a distributed architecture, for which mission designers must also consider collision avoidance, the relative orbits of their spacecraft, as well as the maintenance and reconfiguration of the swarm.

Several authors have directly addressed the problem of spacecraft swarm orbit design. The Integrated Design Engineering and Automation of Swarms system provides an end-to-end mission design architecture with potential application to several scenarios, including planetary moon flybys and Earth observation.[8,9]

[*]Doctoral Candidate, Department of Aeronautics & Astronautics, Stanford University, 496 Lomita Mall, Stanford, California, USA.
[†]Associate Professor, Department of Aeronautics & Astronautics, Stanford University, 496 Lomita Mall, Stanford, California, USA.

However, the system is only applied to the case of inter-spacecraft separations on the scale of constellations and, consequently, has limited application to any mission where collision avoidance within a swarm must be considered. Similarly, a novel swarm mission design methodology was used for the HelioSwarm mission, but application is limited to a specific, P/2 Earth-Moon resonant orbit.[10]

Each of the individual mission design considerations specific to spacecraft swarm missions have been addressed in the literature, either in isolation or in various subsets. The challenge of selecting an appropriate swarm control methodology was addressed from a mission design perspective, however the methods investigated were found to be inefficient in terms of Δv, or were only evaluated for performance in the period immediately following deployment.[11] A proposed swarm guidance and control methodology based on the parameterization of the relative orbit in terms of relative orbital elements (ROE) offers passively bounded relative motion and ensures user-specified minimum separations between all spacecraft.[12] However, direct adaptation of the proposed method to the problem of enabling complete swarm orbit design is infeasible due to its complexity and reliance on convex optimization schemes.

In addition to the limitations already discussed, current methods lack the explainability that is critical for mission designers to understand what trades are available to achieve mission objectives within constraints. Enabling mission designers to understand how their decisions impact key mission parameters will become increasingly important in the future as scientists who are not experts in spacecraft relative guidance, navigation, and control (GNC) seek to avail themselves of the advantages offered by spacecraft swarms. This work will address the limitations in the state of the art by developing a reduced-order model for spacecraft swarm orbit design. The reduced-order model proposed is sufficiently computationally efficient to simulate long-duration missions. It includes (1) swarm configuration, (2) passive and active safety, (3) swarm maintenance and reconfiguration, including the location and timeliness of maneuvers, and (4) delta-v consumption. Additionally, the quantitative impacts of individual design choices are immediately apparent to mission designers.

Following this introduction, the reduced-order model is presented, including a review of the dynamics of spacecraft relative motion. Next, a high-fidelity numerical simulation, which will be used in this paper for validation of the reduced-order model, is described in detail. The SWARM-EX mission is then discussed, with emphasis on how its scientific objectives impose requirements on swarm orbit design. Next, results from the novel reduced-order model are validated through comparison with results obtained in high-fidelity simulation for a set of scenarios that are illustrative of the challenges facing the SWARM-EX mission. Finally, the contributions of this paper are summarized and potential future work is discussed.

REDUCED-ORDER MODEL

In this section, the reduced-order model is presented, beginning with a discussion of the parameterization of spacecraft relative motion and a review of the dynamics of spacecraft relative motion. Next, two methods for achieving swarm reconfigurations are presented, one based on propulsion and the other based on differential atmospheric drag. Finally, a control methodology to ensure both passive and active safety, and to maintain a desired swarm configuration, is introduced. It is important to note that the reduced-order model uses mean absolute and relative orbital elements, as opposed to their osculating counterparts. Osculating absolute and relative orbital elements include short-period dynamics effects, which are not relevant to the design of swarm orbits over long time periods.

Relative Orbit Parameterization

In this paper, two parameterizations of spacecraft relative motion are used. The first parameterization is in terms of ROE. Using ROE permits straightforward visualization of relative orbit geometry, the analytical inclusion of perturbations and maneuvers, as well as the analytical computation of minimum inter-spacecraft separation distances over extended time periods. The ROE are a nonlinear combination of the absolute orbital elements for a chief spacecraft, denoted by the subscript c, and a deputy spacecraft, denoted by the subscript

d, defined as

$$\delta\boldsymbol{\alpha} = \begin{bmatrix} \delta a \\ \delta\lambda \\ \delta e_x \\ \delta e_y \\ \delta i_x \\ \delta i_y \end{bmatrix} = \begin{bmatrix} (a_d - a_c)/a_c \\ (M_d + \omega_d) - (M_c + \omega_c) + (\Omega_d - \Omega_c)\cos(i_c) \\ e_d \cos(\omega_d) - e_c \cos(\omega_c) \\ e_d \sin(\omega_d) - e_c \sin(\omega_c) \\ i_d - i_c \\ (\Omega_d - \Omega_c)\sin(i_c) \end{bmatrix} \tag{1}$$

The relative eccentricity and inclination vectors, $\delta\boldsymbol{e}$ and $\delta\boldsymbol{i}$, can also be represented using polar notation as

$$\delta\boldsymbol{e} = \begin{bmatrix} \delta e_x \\ \delta e_y \end{bmatrix} = \begin{bmatrix} \delta e \cos(\phi) \\ \delta e \sin(\phi) \end{bmatrix} \qquad \delta\boldsymbol{i} = \begin{bmatrix} \delta i_x \\ \delta i_y \end{bmatrix} = \begin{bmatrix} \delta i \cos(\theta) \\ \delta i \sin(\theta) \end{bmatrix} \tag{2}$$

Here δe and δi represent the vector magnitudes, while the phase angles, ϕ and θ are the relative perigee and relative ascending node, respectively. This paper also uses a Cartesian representation of the spacecraft relative position and velocity. To obtain this parameterization of the relative motion, it is first necessary to introduce an additional reference frame. The RTN frame, or Hill orbital frame, provides an intuitive basis from which to observe spacecraft relative motion. The RTN frame is centered on the chief and consists of unit vectors $\hat{o}_r$, aligned with the orbit radial direction, $\hat{o}_n$, normal to the orbital plane and aligned with the chief's angular momentum vector, and $\hat{o}_t$, completing the right-handed triad.

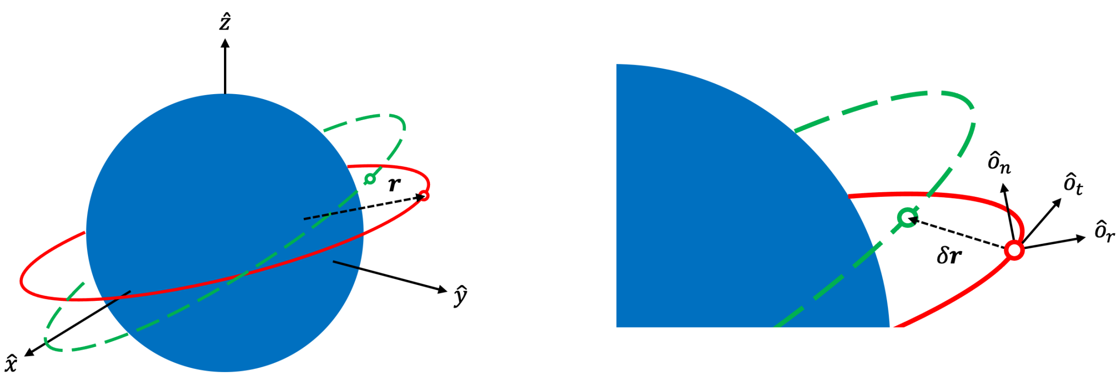

(a) Earth-centered inertial reference frame for absolute orbit parameterization.

(b) RTN reference frame for relative orbit parameterization.

Figure 1: Cartesian reference frames.

The relative position and velocity of a deputy with respect to a chief can be expressed in the RTN frame as

$$\delta\boldsymbol{x} = \begin{bmatrix} \delta r_r \\ \delta r_t \\ \delta r_n \\ \delta v_r \\ \delta v_t \\ \delta v_t \end{bmatrix} = \begin{bmatrix} \Delta\boldsymbol{r} \cdot \hat{o}_r \\ \Delta\boldsymbol{r} \cdot \hat{o}_t \\ \Delta\boldsymbol{r} \cdot \hat{o}_n \\ \Delta\boldsymbol{v} \cdot \hat{o}_r + \Delta\boldsymbol{r} \cdot \dot{\hat{o}}_r \\ \Delta\boldsymbol{v} \cdot \hat{o}_r + \Delta\boldsymbol{r} \cdot \dot{\hat{o}}_t \\ \Delta\boldsymbol{v} \cdot \hat{o}_r + \Delta\boldsymbol{r} \cdot \dot{\hat{o}}_n \end{bmatrix} \tag{3}$$

where the $\Delta(\cdot)$ operator indicates an arithmetic difference and $\boldsymbol{r}$ and $\boldsymbol{v}$ represent Cartesian position and velocity vectors, respectively. For near-circular orbits, the ROE have been shown to be equivalent to the integration constants of the Hill-Clohessy-Wiltshire (HCW) equations.[13] This permits a first-order mapping between ROE and relative position and velocity vectors as

$$\begin{bmatrix}\delta r_r\\ \delta r_t\\ \delta v_r\\ \delta v_t\end{bmatrix} = a_c \begin{bmatrix} 1 & 0 & -\cos(u_c) & -\sin(u_c)\\ 0 & 1 & 2\sin(u_c & -2\cos(u_c)\\ 0 & 0 & n_c\sin(u_c) & -n_c\cos(u_c)\\ -1.5n_c & 0 & 2n_c\cos(u_c) & 2n_c\sin(u_c)\end{bmatrix}\begin{bmatrix}\delta a\\ \delta\lambda\\ \delta e_x\\ \delta e_y\end{bmatrix} \tag{4}$$

$$\begin{bmatrix}\delta r_n\\ \delta v_n\end{bmatrix} = a_c \begin{bmatrix}\sin(u_c) & -\cos(u_c)\\ n_c\cos(u_c) & n_c\sin(u_c)\end{bmatrix}\begin{bmatrix}\delta i_x\\ \delta i_y\end{bmatrix} \tag{5}$$

where the parameter u is the mean argument of latitude, defined as $u = \omega + M$. Comparable relationships between ROE and Cartesian relative motion representations have also been demonstrated in a variety of other orbit regimes. A first-order mapping between relative position in the RTN frame and arithmetic differences of classical Keplerian orbital elements was shown by Casotto and Schaub.[14,15] This has been extended to eccentric orbits by demonstrating an equivalent relationship between ROE and the integration constants of the Yamanaka-Ankersen equations by Sullivan and Guffanti.[16,17] The analysis in this paper is limited to near-circular orbits. Therefore, only the mapping shown in Eqs. 4 and 5 will be used.

By projecting the relative position vector of a deputy with respect to a chief onto the RN plane and expressing the resulting equation in terms of ROE, an expression for the minimum separation distance between the two spacecraft may be obtained as

$$\delta r_{rn}^{min} = \frac{\sqrt{2}a_c|\delta\boldsymbol{e}\cdot\delta\boldsymbol{i}|}{(\delta e^2 + \delta i^2 + |\delta\boldsymbol{e}+\delta\boldsymbol{i}|\cdot|\delta\boldsymbol{e}-\delta\boldsymbol{i}|)^{1/2}} \tag{6}$$

Note that this expression is only valid for the case where $\delta a = 0$, which can be expected for spacecraft swarms under nominal conditions since a non-zero δa results in a secular drift in along-track separation. Inspection of Eq. 6 indicates that, in order to ensure the largest separation between spacecraft, $\delta\boldsymbol{e}$ and $\delta\boldsymbol{i}$ should be (anti-)parallel and have the largest magnitude possible. This leads to the well known concept of e-/i-vector separation to achieve passive safety for spacecraft swarms, which has been employed in multiple spacecraft formation-flying and rendezvous missions, including GRACE, PRISMA, and TanDEM-X.[1–3]

Spacecraft Relative Motion

In unperturbed Keplerian motion, the time derivatives of the absolute orbital elements are zero except for the mean anomaly, which varies as the mean motion, n.

$$\frac{da}{dt} = \frac{de}{dt} = \frac{di}{dt} = \frac{d\Omega}{dt} = \frac{d\omega}{dt} = 0 \qquad\qquad \frac{dM}{dt} = \frac{\mu^{1/2}}{a^{3/2}} = n \tag{7}$$

By applying the terms in Eq. 7 to the definition of the ROE in Eq. 1, it is apparent that the ROE are constant except for the relative mean longitude, which varies with the mean motions of the chief and deputy and experiences a secular drift in the case of a non-zero δa. For the case where $\delta a = 0$, the relative motion of a deputy with respect to a chief is described by an ellipse with semi-major axis $2a\delta e$ and semi-minor axis $a\delta e$ in the RT plane, with the mean along-track separation given by $a\delta\lambda$. Motion in the RN plane is described by a harmonic oscillation with amplitude $a\delta i$.

For spacecraft in low Earth orbit (LEO), the dominant perturbations are J_2 and atmospheric drag. Secular variation of the mean absolute orbital elements due to J_2 can be expressed as[18]

$$\frac{d\boldsymbol{\alpha}}{dt} = \frac{d}{dt}\begin{bmatrix}a\\ e\\ i\\ \Omega\\ \omega\\ M\end{bmatrix} = \kappa\begin{bmatrix}0\\ 0\\ 0\\ -2\cos(i)\\ 5\cos^2(i)-1\\ \eta(3\cos^2(i)-1)\end{bmatrix} \tag{8}$$

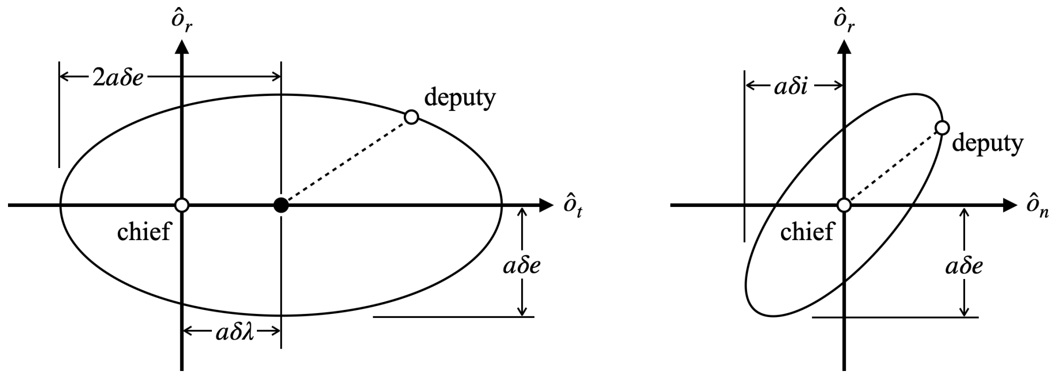

Figure 2: Geometric interpretation of relative orbital elements.

where the parameters η and κ are defined as

$$\eta = (1 - e^2)^{1/2} \qquad\qquad \kappa = \frac{3}{4}\frac{J_2 R_E^2 \mu^{1/2}}{a^{7/2}\eta^4}$$

By substituting into the definition of the ROE given in Eq. 1, the secular variation of the mean ROE due to J_2 can be expressed as[19]

$$\begin{aligned}\frac{d\delta\boldsymbol{\alpha}}{dt} = \kappa_d &\begin{bmatrix} 0 \\ \eta_d(3\cos^2(i_d) - 1) + (5\cos^2(i_d) - 1) - 2\cos(i_d)\cos(i_c) \\ -e_d \sin(\omega_d - \omega_c)(5\cos^2(i_d) - 1) \\ e_d \cos(\omega_d - \omega_c)(5\cos^2(i_d) - 1) \\ 0 \\ -2\cos(i_d)\sin(i_c) \end{bmatrix} \\ - \kappa_c &\begin{bmatrix} 0 \\ (1 + \eta_c)(3\cos^2(i_c) - 1) \\ -e_d \sin(\omega_d - \omega_c)(5\cos^2(i_c) - 1) \\ e_d \cos(\omega_d - \omega_c)(5\cos^2(i_c) - 1) \\ 0 \\ -2\cos(i_c)\sin(i_c) \end{bmatrix}\end{aligned} \tag{9}$$

By assuming that the orbits are near-circular, and that the distance between the chief and deputy are much smaller than either spacecraft's distance to the central body, the expressions in Eq. 9 can be simplified considerably to

$$\frac{d\delta\boldsymbol{\alpha}}{dt} = \begin{bmatrix} 0 \\ -7\kappa_c \sin(2i_c)\delta i_x \\ -\kappa_c(5\cos^2(i_c) - 1)\delta e_y \\ \kappa_c(5\cos^2(i_c) - 1)\delta e_x \\ 0 \\ 2\kappa_c \sin^2(i_c)\delta i_x \end{bmatrix} \tag{10}$$

Under this simplified model, the effects of J_2 on the ROE are a secular drift in $\delta\lambda$ and the δi_y, both proportional to δi_x, and a rotation of $\delta\boldsymbol{e}$. The rate at which $\delta\boldsymbol{e}$ rotates, the time derivative of the relative perigee, ϕ, can be expressed as

$$\frac{d\phi}{dt} = \kappa_c(5\cos^2(i_c) - 1) \tag{11}$$

which is also equivalent to the time derivative of the absolute argument of periapsis, $\dot{\omega}$.[12] These effects are summarized in Figure 3.

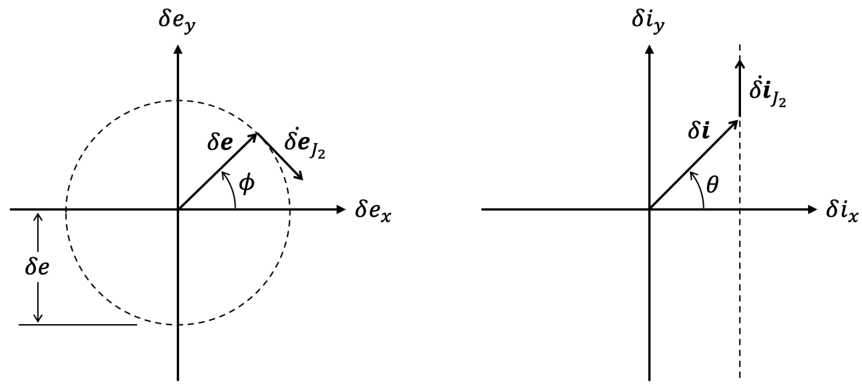

Figure 3: Effect of J_2 on relative eccentricity and inclination vectors.

Spacecraft operating in LEO experience an acceleration acting in the anti-flight direction due to atmospheric drag. This acceleration may be modeled as

$$p_{drag} = \frac{1}{2}\rho v^2 B \tag{12}$$

where ρ is the atmospheric density, v is the spacecraft's velocity, and B is the spacecraft's ballistic coefficient. The ballistic coefficient is defined in terms of the drag coefficient, C_D, cross-sectional area, A, and mass, m, of the spacecraft as

$$B = \frac{C_D A}{m} \tag{13}$$

Consistent with the previous assumption of near-circular orbits, the spacecraft's velocity, v may be approximated as

$$v = na \tag{14}$$

The expression in Eq. 12 can then be rewritten as

$$p_{drag} = \frac{1}{2}\rho a^2 n^2 B \tag{15}$$

The effect of atmospheric drag on spacecraft relative orbits is a function of the relative ballistic coefficient between spacecraft, ΔB. This can vary due to a variety of factors, including spacecraft attitudes and propellant expenditure. The relative ballistic coefficient may be computed as

$$\Delta B = B_d - B_c \tag{16}$$

From the Gauss Variational Equations (GVE), an expression for the effect on the ROE of a relative acceleration, $\delta \boldsymbol{p}$, applied to a deputy in the RTN frame may be obtained as[12]

$$\frac{d\delta\boldsymbol{\alpha}}{dt} = \frac{1}{an}\begin{bmatrix} 0 & 2 & 0 \\ -2 & 0 & 0 \\ \sin(u_c) & 2\cos(u_c) & 0 \\ -\cos(u_c) & 2\sin(u_c) & 0 \\ 0 & 0 & \cos(u_c) \\ 0 & 0 & \sin(u_c) \end{bmatrix} \begin{bmatrix} \delta p_r \\ \delta p_t \\ \delta p_n \end{bmatrix} \tag{17}$$

Considering that atmospheric drag acts solely in the anti-flight direction, the time derivative of δa is then given by

$$\frac{d\delta a}{dt} = \rho a n \Delta B \tag{18}$$

which shows a linear drift. This linear drift results in a quadratic accumulation of along-track separation as

$$\frac{d\delta\lambda}{dt} = \frac{3}{2}\rho a n^2 \Delta B t \tag{19}$$

Although only perturbations of spacecraft relative motion due to J_2 and atmospheric drag are considered in this paper, the parameterization of the relative motion in terms of ROE also permits the analytical inclusion of additional perturbations, including solar radiation pressure.[20]

Swarm Reconfiguration

Similarly to Eq. 17, an expression for the change in ROE due to an instantaneous velocity increment applied to a deputy in the RTN frame may be obtained as

$$\Delta\delta\boldsymbol{\alpha} = \frac{1}{an}\begin{bmatrix} 0 & 2 & 0 \\ -2 & 0 & 0 \\ \sin(u_c) & 2\cos(u_c) & 0 \\ -\cos(u_c) & 2\sin(u_c) & 0 \\ 0 & 0 & \cos(u_c) \\ 0 & 0 & \sin(u_c) \end{bmatrix}\begin{bmatrix} \Delta v_r \\ \Delta v_t \\ \Delta v_n \end{bmatrix} \tag{20}$$

where in-plane and out-of-plane control are decoupled. As demonstrated by the PRISMA and TanDEM-X missions, control of δa, $\delta\lambda$, and $\delta\boldsymbol{e}$ can be achieved using pairs of equal and opposite impulsive maneuvers in the tangential direction. Individual impulsive maneuvers in the normal direction can be used to control $\delta\boldsymbol{i}$. The reduced-order model is based on this particular control methodology because it is simple and has extensive flight heritage.

More importantly to mission designers than the specific control methodology used, however, is the associated Δv cost. The lower bound for the Δv cost of an in-plane reconfiguration between an initial set of ROE, $\delta\boldsymbol{\alpha}_0$, and a final set of ROE, $\delta\boldsymbol{\alpha}_1$, can be computed as[21]

$$\frac{\Delta v_{\text{in-plane}}}{n a_c} = \max\left(\frac{|\Delta\delta a|}{2}, \frac{|\Delta\delta\lambda|}{3\Delta t}, \frac{\|\Delta\delta\boldsymbol{e}\|}{2}\right) \tag{21}$$

where $\Delta\delta(\cdot) = \delta(\cdot)_1 - \delta(\cdot)_0$, Δt is time between the first and second maneuvers of the pair, and $\|\cdot\|$ represents the L^2 norm. Note that the reduced-order model does not consider reconfigurations of δa, and so only the second and third terms of the right-hand side of Eq. 21 will be used. The time dependency for along-track reconfiguration provides mission designers with a trade between the speed of a reconfiguration and its Δv cost. From Eq. 21, it is apparent that, for a given along-track reconfiguration, the time permitted for the reconfiguration is inversely proportional to the Δv cost. This inverse relationship can be explained through a description of the control methodology for along-track reconfiguration using propulsion.

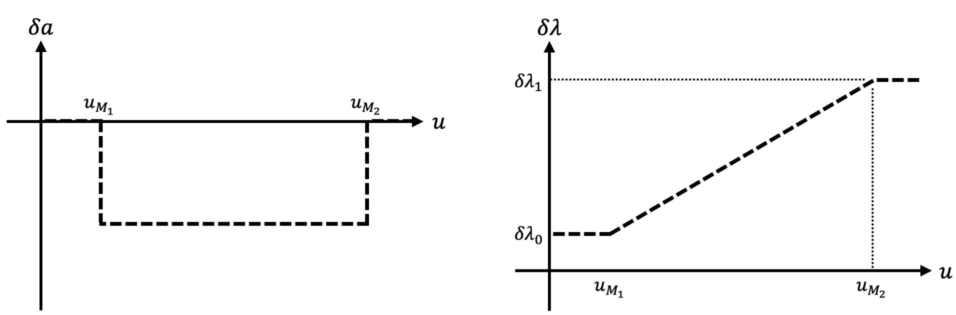

Figure 4: Change in δa and $\delta\lambda$ during propulsive reconfiguration.

First, a tangential maneuver at $u = u_{M_1}$ introduces a difference in δa, resulting in a linear drift in $\delta\lambda$. After a waiting period, Δt, the desired value of $\delta\lambda$ is reached. A second tangential maneuver at $u = u_{M_2}$

corrects the difference in δa, arresting the drift. By expending more propellant, a larger initial difference in δa is introduced, and subsequently corrected, increasing the drift rate and resulting in a shorter waiting period to realize the same change in $\delta\lambda$.

Out-of-plane reconfiguration is achieved using a single impulsive maneuver in the normal direction. The lower bound for the Δv cost of this reconfiguration can be computed as[21]

$$\frac{\Delta v_{\text{out-of-plane}}}{n a_c} = \|\Delta \delta \boldsymbol{i}\| \tag{22}$$

The process for computing the total Δv cost of a swarm reconfiguration, including in-plane and out-of-plane components, is described in Algorithm 1.

Algorithm 1 Computation of Swarm Reconfiguration Δv Cost

function computeDeltavReconfiguration($\delta\boldsymbol{\alpha}_0, \delta\boldsymbol{\alpha}_1, \Delta t, a_c$)
  $\Delta\delta\lambda = |\delta\lambda_1 - \delta\lambda_0| \leftarrow$ Compute desired change in $\delta\lambda$
  $\Delta\delta e = |\delta e_1 - \delta e_0| \leftarrow$ Compute desired change in δe
  $\Delta v_{\text{in-plane}} \leftarrow$ Compute in-plane reconfiguration cost (Eq. 21)
  $\Delta\delta i = |\delta i_1 - \delta i_0| \leftarrow$ Compute desired change in δi
  $\Delta v_{\text{out-of-plane}} \leftarrow$ Compute out-of-plane reconfiguration cost (Eq. 22)
  $\Delta v_{\text{reconfig}} = \Delta v_{\text{in-plane}} + \Delta v_{\text{out-of-plane}}$
  return $\Delta v_{\text{reconfig}}$

As suggested by Eqs. 17, 18, and 19, atmospheric drag may also be used to control in-plane spacecraft relative motion. The use of atmospheric drag for control is particularly attractive because it does not require the expenditure of valuable propellant. Control using differential drag has been demonstrated in orbit for small satellites and will undoubtedly continue to mature as a control methodology in the future.[22] The reduced-order model allows mission designers the flexibility to choose between using propulsion or differential drag to realize along-track reconfigurations. Along-track reconfigurations using differential drag require that the spacecraft in a swarm be capable of introducing a relative ballistic coefficient. Typically, this is achieved through attitude control, with a spacecraft varying its cross-sectional area as viewed from the velocity direction. Although control of $\delta \boldsymbol{e}$ is also possible through differential drag, this is not included in the reduced-order model.

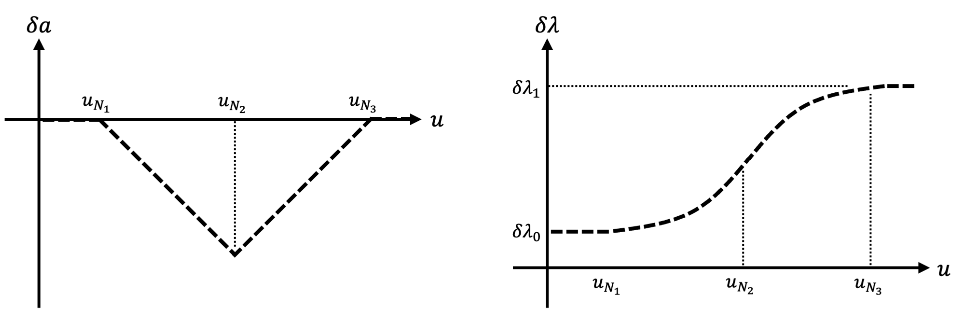

Figure 5: Change in δa and $\delta\lambda$ during differential drag reconfiguration.

The process of achieving an along-track reconfiguration using differential drag begins when the spacecraft introduce a relative ballistic coefficient at $u = u_{N_1}$. This causes a linear drift in δa, as described in Eq. 18, and a corresponding quadratic accumulation in $\delta\lambda$. This relative ballistic coefficient is maintained until approximately half of the desired change in $\delta\lambda$ has been achieved, at $u = u_{N_2}$. At this point, the spacecraft adjust their attitudes such that the relative ballistic coefficient now has the same magnitude but opposite sign. This causes the linear drift in δa to reverse direction and trend towards zero, ideally reaching zero just as the desired value of $\delta\lambda$ is reached, at u_{N_3}.

In contrast to along-track reconfiguration using propulsion, mission designers are not able to choose the amount of time that will be allowed for reconfiguration when using differential drag. Instead, they are able to select ΔB, which is dependent on a variety of factors, including the physical design of spacecraft and any attitude constraints. To determine the time required to perform an along-track reconfiguration using differential drag, begin with the expression for the change in $\delta\lambda$ due to a secular drift in δa, given by

$$\Delta\delta\lambda = \frac{3}{4}n\frac{d\delta a}{dt}\Delta t^2 \tag{23}$$

Using Eq. 18 and rearranging to isolate Δt gives

$$\Delta t = \sqrt{\frac{4\Delta\delta\lambda}{3\rho n^2 a\Delta B}} \tag{24}$$

The expression in Eq. 24 represents only part of an along-track reconfiguration, however, since an offset in δa at the end of a maneuver is not desirable. As shown in Figure 5, the maneuver must be performed in two parts, during each of which approximately half of the total desired change in $\delta\lambda$ is achieved. Thus, the amount of time required to perform a complete along-track reconfiguration may be computed as

$$\Delta t_{\delta\lambda} = \sqrt{\frac{8\Delta\delta\lambda}{3\rho n^2 a\Delta B}} \tag{25}$$

It should be noted that the Δv costs presented in this section are lower bounds, and do not account for sources of error such as navigation uncertainty or maneuver execution errors. Mission designers should add an appropriate margin to these Δv costs for planning purposes.

Swarm Maintenance

The reduced-order model uses the method of e-/i-vector separation for swarm maintenance by leveraging knowledge of the secular evolution of the ROE due to perturbations. This methodology is based on defining control windows around the nominal relative e-/i-vectors. The sizes of these control windows, δe_{max} and δi_{max}, are parameters that may be chosen by mission designers. The e-/i-vectors follow predictable paths, depicted by the dotted lines in Figure 6. When, for example, $\delta\boldsymbol{e}$ reaches the edge of its control window at $\delta\boldsymbol{e}^{pre}$, a pair of maneuvers is executed in order to shift the vector to the opposite edge of the control window, at $\delta\boldsymbol{e}^{post}$. This minimizes the frequency of maneuvers that are performed while maintaining a passively safe e-/i-vector separation.

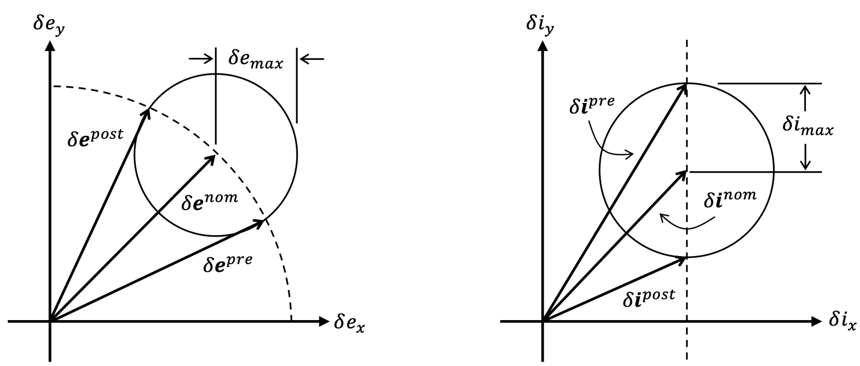

Figure 6: Swarm maintenance nominal e-/i-vectors and control windows.

From Eq. 6, it is possible to compute the minimum inter-spacecraft separation for a given relative orbit. However, this equation is only valid at a single instant, while the e-/i-vectors vary in time and can potentially fall anywhere within the control window bounds over long time periods. Mission designers must know what is the worst case minimum inter-spacecraft separation for a given nominal relative orbit and set of control window bounds. To find this, begin by computing the maximum allowed deviation of the relative perigee, $\delta\phi$ as

$$\delta\phi = \arcsin\left(\frac{\delta e_{max}}{\|\delta\boldsymbol{e}^{nom}\|}\right) \tag{26}$$

The pre- and post-maneuver relative eccentricity vectors can then be obtained by rotating $\delta\boldsymbol{e}^{nom}$ about the z-axis by $+\delta\phi$ and $-\delta\phi$. For $\delta\boldsymbol{i}$, the pre- and post-maneuver vectors can be computed as

$$\delta\boldsymbol{i}^{pre} = \begin{bmatrix} \delta i_x^{nom} \\ \delta i_y^{nom} + \text{sign}(\delta i_x^{nom})\delta i_{max} \end{bmatrix} \qquad \delta\boldsymbol{i}^{post} = \begin{bmatrix} \delta i_x^{nom} \\ \delta i_y^{nom} - \text{sign}(\delta i_x^{nom})\delta i_{max} \end{bmatrix} \tag{27}$$

Next, a check is performed to determine if it is possible to form a right angle within the region swept by $\delta\boldsymbol{e}$ and $\delta\boldsymbol{i}$. This may be accomplished by computing the angles between each of the four possible combinations of pre- and post-maneuver e-/i-vectors. If the minimum of this set is less than 90° and the maximum is greater than 90°, then the worst-case minimum separation is zero, indicating that a conjunction is possible. Otherwise, the worst-case minimum separation will occur at one of the extremes. Returning to the pre- and post-maneuver e-/i-vectors, Eq. 6 is used to compute the minimum separation for each of the four possible combinations. Finally, the worst-case minimum separation is found by choosing the minimum of that set.

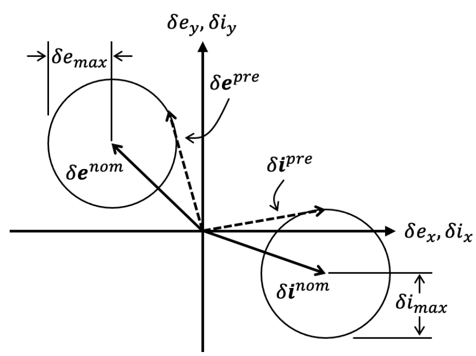

Figure 7: Determination of minimum inter-spacecraft separation over long time periods.

For the example shown in Figure 7, it is not possible to form a 90° angle. By visual inspection, the worst case relative configuration occurs when $\delta\boldsymbol{e}$ reaches $\delta\boldsymbol{e}^{pre}$ and $\delta\boldsymbol{i}$ reaches $\delta\boldsymbol{i}^{pre}$. The process of computing the worst-case minimum inter-spacecraft separation is described in detail in Algorithm 2.

Algorithm 2 Computation of the Minimum Inter-Spacecraft Separation

function computeMinimumSeparation($\delta\boldsymbol{e}^{nom}$,$\delta e_{max}$,$\delta\boldsymbol{i}^{nom}$,$\delta i_{max}$)
  $\delta\phi \leftarrow$ Compute maximum deviation in ϕ (Eq. 26)
  $\delta\boldsymbol{e}^{pre}, \delta\boldsymbol{e}^{post} \leftarrow$ Compute pre- and post-maneuver $\delta\boldsymbol{e}$
  $\delta\boldsymbol{i}^{pre}, \delta\boldsymbol{i}^{post} \leftarrow$ Compute pre- and post-maneuver $\delta\boldsymbol{i}$ (Eq. 27)
  for $m \in \{pre, post\}$
    for $n \in \{pre, post\}$
      $\psi^{mn} \leftarrow$ Compute angle between $\delta\boldsymbol{e}^m$ and $\delta\boldsymbol{i}^n$
      $\delta r_{rn}^{mn} \leftarrow$ Compute minimum separation between $\delta\boldsymbol{e}^m$ and $\delta\boldsymbol{i}^n$ (Eq. 6)
  if min$(\psi^{mn}) < 90°$ **and** max$(\psi^{mn}) > 90° \ \forall\, m, n$
    $\delta r_{rn}^{min} = 0$
  else
    $\delta r_{rn}^{min} = \min(\delta r_{rn}^{mn}) \ \forall\, m, n$
  return δr_{rn}^{min}

Another attractive feature of the method of e-/i-vector separation is that the locations of maneuvers are highly deterministic. The location of the first maneuver in a pair for in-plane swarm maintenance may be computed as

$$u_{M_1} = \arctan\left(\frac{\delta e_y^{post} - \delta e_y^{pre}}{\delta e_x^{post} - \delta e_x^{pre}}\right) \tag{28}$$

while the maneuver of the second in-plane maneuver, u_{M_2} is simply computed as $u_{M_2} = u_{M_1} + \pi$. The location of the single out-of-plane impulsive maneuver, u_M can be computed as

$$u_M = \arctan\left(\frac{\delta i_y^{post} - \delta i_y^{pre}}{\delta i_x^{post} - \delta i_x^{pre}}\right) \tag{29}$$

In addition to knowing where within an orbit maneuvers will be performed, it is important for mission designers to understand how frequently pairs of in-plane or individual out-of-plane swarm maintenance maneuvers must be performed. The e-/i-vectors will trace out their full path, as determined by the size of the control windows, before corrective action is taken. By computing the lengths of those paths the maneuver frequency can be approximated. The time between pairs of in-plane maneuvers is given by

$$\Delta t_{\delta e} = \frac{2\delta\phi + \pi\dot{\phi}}{\dot{\phi}} \tag{30}$$

where $2\delta\phi$ gives the angular path covered by the relative eccentricity vector as it moves from one edge of the control window to the other and $\pi\dot{\phi}$ gives the rotation experienced by $\delta\boldsymbol{e}$ during the period between the two tangential maneuvers. Similarly, the time between individual out-of-plane maneuvers is given by

$$\Delta t_{\delta i} = \frac{2\delta i_{\text{max}}}{\dot{\delta i}_y} \tag{31}$$

The minimum of $\Delta t_{\delta e}$ and $\Delta t_{\delta i}$ is then the driver of swarm maintenance maneuver frequency, given by

$$\Delta t_{\text{maneuver}} = \min\left(\Delta t_{\delta e},\ \Delta t_{\delta i}\right) \tag{32}$$

Finally, mission designers must be able to estimate the Δv cost of swarm maintenance over extended time periods. This Δv cost can be approximated by assuming that, over a time period, Δt, all secular drift of the e-/i-vectors must be corrected. Although this correction is actually performed incrementally, the computation of the Δv cost is a function only of the magnitude of the correction and does not consider how it is discretized. Thus, by computing the total secular drift over Δt and then computing the cost of correcting that drift, the Δv cost may be approximated as

$$\frac{\Delta v_{\text{in-plane}}}{n a_c} = \dot{\phi}\Delta t \frac{\|\delta \boldsymbol{e}^{nom}\|}{2} \tag{33}$$

for in-plane swarm maintenance. Out-of-plane maintenance cost can similarly be computed as

$$\frac{\Delta v_{\text{out-of-plane}}}{n a_c} = \dot{\delta i}_y \Delta t \tag{34}$$

The total cost of swarm maintenance is then given by

$$\Delta v_{\text{total}} = \Delta v_{\text{in-plane}} + \Delta v_{\text{out-of-plane}} \tag{35}$$

Although the presentation of the reduced-order model has thus far been limited to a pair of spacecraft, its extension to larger numbers of spacecraft is possible with minimal effort. There are multiple methods by which this may be accomplished. One possible method is to separate all spacecraft in the swarm in the along-track sense and have each control their relative orbit with respect to a common reference. If more flexibility is needed, Koenig has proposed a method by which the general concept of e-/i-vector separation may be extended to arbitrarily large spacecraft swarms.[12] For the purposes of the reduced-order model, simply repeat the calculations for each individual spacecraft with respect to the common reference, or, if needed, with respect to each pair in the swarm.

HIGH-FIDELITY NUMERICAL SIMULATION

While the reduced-order model presented in the previous section provides information that is essential to the design of spacecraft swarm orbits, the information cannot be expected to have the same level of accuracy as that which may be obtained through high-fidelity numerical simulation. Instead, the low computational complexity of the reduced-order model permits the rapid simulation of missions lasting for months, which is infeasible for high-fidelity simulation. However, a reduced-order model is only valuable if the information it provides is sufficiently accurate. In order to demonstrate that the reduced-order model meets this criteria, its outputs must be validated through comparison with some "reference truth". In this section, the high-fidelity simulation that will serve as the reference truth is presented.

Space Rendezvous Laboratory Satellite Software

The Space Rendezvous Laboratory Satellite Software ($\mathcal{S}^3$) is a custom software library which includes modules for numerical orbit propagation, orbit and attitude perturbation modeling, reference system transformation, and time system conversion.[23] The underlying software is written in C++ to enable speed and portability. Additionally, S-function and MEX function wrappers allow $\mathcal{S}^3$ to be used within a MATLAB/Simulink environment.

Table 1: High-fidelity simulation force models and corrections.

Perturbation/Transformation	**Model**
Equations of motion	Gauss variational equations
Numerical integrator	Fourth-order Runge-Kutta[24] Richardson extrapolation[25]
Gravity field	GRACE Gravity Model GGM01S (120x120)[26]
Atmospheric drag	NRLMSISE-00[24] Cannonball spacecraft model[24]
Solar radiation pressure	Flat plate model[24] Conical Earth shadow model[24]
Geomagnetic and solar flux data	NOAA daily KP AP indices
Third-body perturbation	Analytical Sun and Moon[24]
Relativistic corrections	First-order corrections for special and general relativistic effects[24]

The performance of $\mathcal{S}^3$ has been validated extensively through comparison with flight products from the PRISMA mission. For the subsequent analysis in this paper, the force models and perturbations shown in Table 1 are used.

Simulation Guidance, Navigation, and Control

In addition to those perturbations summarized in Table 1, the high-fidelity simulation includes navigation and maneuver execution errors. Navigation error is modeled as zero mean, white Gaussian noise that is added to the reference truth ROE state, with standard deviation based on flight results from the TanDEM-X mission.[3] Maneuver execution errors are modeled through multiple sources. First, the combination of the discretization of the simulation time interval and navigation errors ensure that maneuvers are not executed at the "ideal" time. Second, white Gaussian noise is added to planned maneuver vectors in the RTN frame. This simulates errors in both the magnitude and direction of maneuvers due to imperfect thruster and attitude control.

SWARM-EX MISSION AND REQUIREMENTS

The SWARM-EX mission consists of three 3U CubeSats operating in LEO. Each spacecraft is equipped with a self-contained attitude determination and control system (ADCS) and a cold gas propulsion unit, consisting of a single thruster and propellant tank. The ADCS enables 3-axis attitude control, and, in combination with the propulsion unit, allows SWARM-EX spacecraft to perform propulsive maneuvers in any direction. The GNC software onboard each spacecraft consists of a navigation module and a control module. The navigation module uses an unscented Kalman filter to estimate absolute orbital elements and ROE, as well as auxiliary parameters. The control module is based on the method of e-/i-vector separation but also includes a novel hybrid propulsive/differential drag control scheme for experimental purposes.[27]

SWARM-EX has an ambitious set of scientific and engineering objectives meant to address outstanding questions in aeronomy and to advance the state of the art in spacecraft swarming and related technologies. The spacecraft use deployable solar panels, resulting in a maximum cross-sectional area that is approximately nine times their minimum cross-sectional area, as shown in Figure 8.

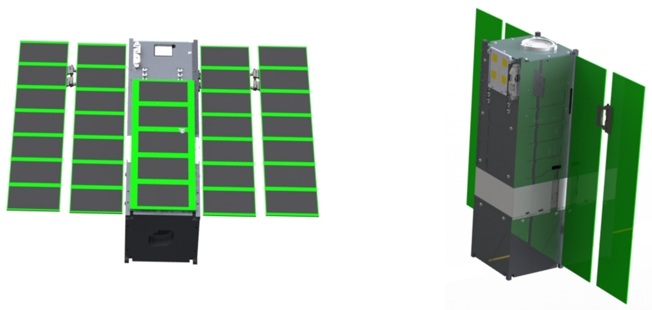

Figure 8: Digital rendering of SWARM-EX spacecraft structural design.

This significant difference in the achievable cross-sectional areas motivates the use of control through differential drag, and enables a novel experiment in which the spacecraft themselves will be used as a distributed aeronomy sensor. In this experiment, the ballistic coefficients of SWARM-EX spacecraft will be modulated to increase the sensitivity of their relative motion to atmospheric drag. Through simultaneous, precise estimation of the spacecraft relative motion and environmental parameters, atmospheric mass density will be recovered. The scientific objectives are focused on the equatorial ionization anomaly (EIA) and equatorial thermospheric anomaly (ETA), features of the ionized region of the upper atmosphere. Using Flux-Probe-Experiment and Langmuir probe sensors, SWARM-EX will make in-situ measurements of plasma and neutral densities in the EIA and ETA at a variety of spatial and temporal scales. The mission objectives are divided into a set of primary science questions (PSQ) and secondary measurement demonstrations (SMD).

Table 2: Summary of high-level SWARM-EX mission objectives.

Primary Science Questions	
PSQ-1	How persistent and correlated are the plasma density and neutral density in the EIA and ETA features?
PSQ-2	Over what timescales ($<$ 90 min) do we observe changes in the EIA and ETA properties due to non-migrating tides and geomagnetic activity?
Secondary Measurement Demonstrations	
SMD-1	Cross-calibrate the plasma and AO measurements from each spacecraft
SMD-2	Demonstrate horizontal plasma gradient density measurements as scales of $\leq$ 10 km
SMD-3	Demonstrate the ability to estimate mass density by observing the relative motion of two spacecraft
SMD-4	Demonstrate estimation of density gradients at vertical scales $\geq$ 10 km

Each PSQ and SMD is further subdivided into one or more measurement objectives. These measurement objectives are then translated into requirements for the absolute and relative orbits, as shown in Table 3.

Table 3: Sample of SWARM-EX measurement objectives and corresponding orbit requirements.

	Measurement Objective	**Orbit Requirement**
PSQ-1.B	Make dayside observations of plasma density over $\pm 20°$ from the magnetic equator	$50° < i < 130°$
PSQ-1.D	Simultaneously observe the southern crest, northern crest, and trough of the EIA and ETA	Mean along track separation 1300 ± 100 km while in target region
PSQ-1.E	Make observations at altitudes > 400 km and $<$ 450 km	6798.137 km $< a <$ 6853.137 km at deployment
SMD-3	Measure relative velocity of two spacecraft over a 1-week period	Mean along-track separation ≤ 100 km and maximum radial separation ≤ 10 km
SMD-4	Measure plasma and neutral densities with vertical distances between sensors ≥ 10 km over a 1-week period	Mean along-track separation $\leq$ 10 km and maximum radial separation $\geq$ 10 km while in target region

In order to achieve its objectives, SWARM-EX must realize a variety of relative orbits, including along-track separations ranging from hundreds of meters to thousands of kilometers. The development of the reduced-order model proposed in this paper was specifically motivated by the need to provide accurate information to SWARM-EX mission designers. Important questions arose early in the mission development process about Δv consumption, safety, and other key mission parameters that could not be satisfactorily answered using existing models and methods.

Analysis performed using the reduced-order model has informed many aspects of the SWARM-EX mission design, including Δv budgeting and concept of operations development, the selection of onboard communications hardware, and the physical size of propellant tanks. For example, the accomplishment of SMD-4 requires the introduction of a radial separation ≥ 10 km between spacecraft, necessitating a large out-of-plane reconfiguration. Once informed of the high estimated Δv cost of this reconfiguration, mission designers decided to move SMD-4 into the extended mission phase so as not to jeopardize other, higher priority mission objectives.

The diversity of its mission objectives and the corresponding orbit requirements make SWARM-EX emblematic of the future of spacecraft swarms. Therefore, all subsequent analysis in this paper is performed with reference to the SWARM-EX mission.

RESULTS

In this section, two scenarios are presented which are illustrative of the challenges faced by SWARM-EX. Each scenario is evaluated using both the reduced-order model and high-fidelity simulation. Performance of the reduced-order model is then validated through comparison of the two sets of results. The first scenario is focused on swarm reconfiguration, and demonstrates how mission designers can approach the problem of performing along-track reconfigurations. The second scenario is focused on swarm maintenance, and demonstrates how mission designers can use the reduced-order model to address safety, Δv consumption, and maneuver timeliness over long time periods.

Table 4: SWARM-EX spacecraft simulation parameters.

Parameter	Mass	C_D	A_D		C_R	A_{SRP}
Value	5.0 kg	2.2	0.010 m^2 (low-drag)	0.025 m^2 (high-drag)	0.2	0.040 m^2

For consistency, the spacecraft parameters are held constant throughout this analysis for both the reduced-order model and the high-fidelity simulation. Note that the cross-sectional area, A_D, is chosen based on whether a spacecraft is in a low-drag or high-drag attitude. Although the SWARM-EX spacecraft have an achievable cross-sectional area of up to 0.090 m^2, there are a variety of constraints which make maintaining this attitude for extended time periods infeasible.[28] Instead, the high-drag value shown in Table 4 is chosen conservatively. Additionally, because solar radiation pressure is not included in the reduced-order model, C_R and A_{SRP} are only used in the high-fidelity simulation.

Swarm Reconfiguration

In this scenario, two SWARM-EX spacecraft perform a reconfiguration using either propulsion or differential drag. The chief's initial mean absolute orbital elements are given by

$$\boldsymbol{\alpha}_c = [6853.137\text{ km}, 0.0001, 51.6°, 28.0°, 65.0°, 47.0°]^T \tag{36}$$

the initial set of nominal ROE is given by

$$a\delta\boldsymbol{\alpha}_0^{nom} = [0, 1000, 0, 1000, 0, 1000]^T \text{ m} \tag{37}$$

and the desired set of ROE after reconfiguration is given by

$$a\delta\boldsymbol{\alpha}_1^{nom} = [0, 5000, 0, 1000, 0, 1000]^T \text{ m} \tag{38}$$

representing an increase in the mean along-track separation of 4 km.

Propulsive Reconfiguration As previously discussed, when realizing an along-track reconfiguration using propulsion, the time duration of the reconfiguration is a parameter that is chosen by the mission designer. For this scenario, the allowed reconfiguration duration, Δt, is given by

$$\Delta t = 16.0 \text{ orbits} \tag{39}$$

Due to the modeling of navigation and maneuver execution errors in the high-fidelity simulation, it is expected that performing a large number of simulation runs will give a distribution of results for the reconfiguration duration and Δv cost. However, these error sources are not modeled directly in the reduced-order model. Using Algorithm 1, with inputs given by Eqs. 36-39, the reduced-order model instead produces a single result for $\Delta v_{\text{reconfig}}$. By approximating the effects of navigation and maneuver execution errors in the reduced-order model, a more meaningful comparison could be made with the high-fidelity simulation. To achieve this, a large number runs of the reduced-order model are performed while sampling from normal distributions for Δt and for the mean along-track separation at the end of the reconfiguration, $a\delta\lambda_1$.

Performing 1000 runs each of the high-fidelity simulation and the reduced-order model gives the distributions of results shown in Figure 9, where each triangle or circle represents a single simulation run for the high-fidelity simulation or reduced-order model, respectively. For clarity, 3-σ bounds are also included for the high-fidelity simulation (dashed line) and reduced-order model (solid line). As shown, only a small number of reduced-order model runs lie outside the 3-σ bounds for the high-fidelity simulation.

Table 5: Error statistics for propulsive reconfiguration scenario.

	Error Mean	**Error Std Dev** (1-σ)
$\Delta v_{\text{reconfig}}$ [cm/s]	0.04 (1.48%)	0.03 (1.14%)
Δt [# orbits]	0.20 (1.24%)	0.15 (0.94%)

Using the mean value of the results obtained through high-fidelity simulation as the reference truth, errors are computed by taking the difference between that value and each individual run of the reduced-order model. These errors are summarized in Table 5. This result demonstrates that, although there is a range of possible outcomes for a given reconfiguration, the reduced-order provides an excellent approximation of the Δv cost and the time required for that reconfiguration.

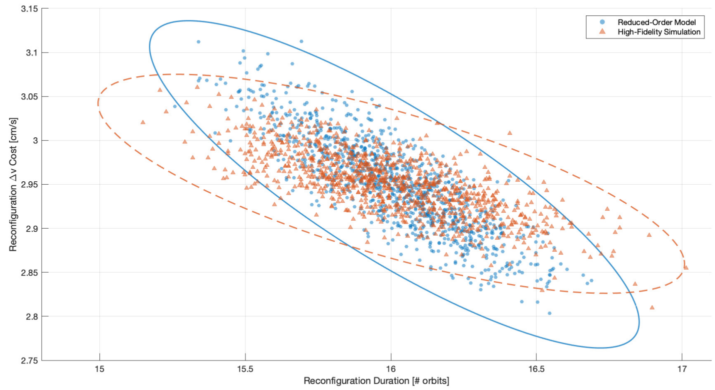

Figure 9: Swarm reconfiguration results using propulsion.

Differential Drag Reconfiguration For along-track reconfigurations using differential drag, the time duration of the reconfiguration, $\Delta t_{\delta\lambda}$ is not a parameter that mission designers are able to choose. Instead, $\Delta t_{\delta\lambda}$ is a key output of the reduced-order model. Drag-based reconfiguration maneuvers are highly sensitive to atmospheric density, ρ. From Eq. 25, the computation of $\Delta t_{\delta\lambda}$ relies on a constant value for ρ. The selection the value of ρ used in the reduced-order model must be based on several factors, including the orbit altitude and expected solar activity during the mission. In this scenario, the value of ρ used in the reduced-order model is the mean of the atmospheric density experienced by the spacecraft in the high-fidelity simulation.

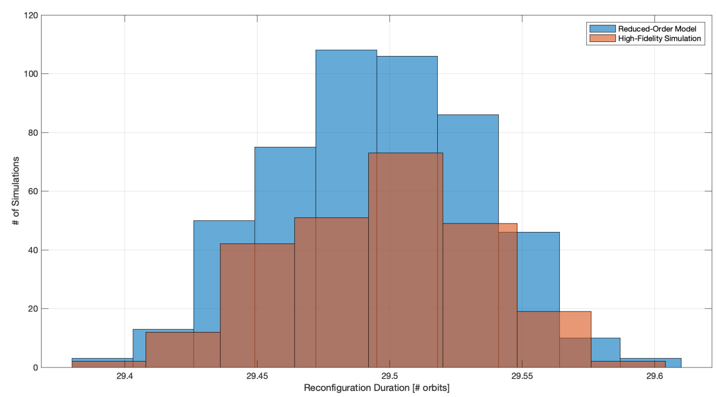

Figure 10: Swarm reconfiguration results using differential drag.

Performing 500 runs of the reduced-order model and 250 runs of the high-fidelity simulation for the reconfiguration defined by Eqs. 37 and 38 provides the distributions for $\Delta t_{\delta\lambda}$ shown in Figure 10. As before, the high-fidelity simulation produces a distribution of results due to navigation and maneuver execution errors. In order to approximate these effects in the reduced-order model, the mean along-track separation at the end of the reconfiguration, $a\delta\lambda_1$, is sampled from a normal distribution.

Table 6: Error statistics for differential drag reconfiguration scenario.

	Error Mean	**Error Std Dev** (1-σ)
$\Delta t_{\delta\lambda}$ [# orbits]	0.029 (0.10%)	0.021 (0.07%)

The result of computing errors using the methodology from the previous scenario is shown in Table 6. For reconfiguration using differential drag, the reduced-order model provides results which are comparable to those obtained through high-fidelity simulation. With careful selection of ρ, mission designers can be confident in the values for $\Delta t_{\delta\lambda}$ provided by the reduced-order model.

Swarm Maintenance

In this scenario, two SWARM-EX spacecraft maintain a desired swarm configuration for a period of approximately 100 orbits. The initial mean absolute orbital elements of the chief are given by Eq. 36. The set of nominal ROE to be maintained is given by

$$a\delta\boldsymbol{\alpha}^{\text{nom}} = [0, 1000, 0, 1000, 0, 1000]^T \text{ m} \tag{40}$$

The sizes of the control windows for the relative e-/i-vectors are given by

$$\delta e_{\text{max}} = \delta i_{\text{max}} = 100 \text{ m} \tag{41}$$

As before, a distribution of results is expected for Δv_{total} and δr_{rn}^{min}. In this scenario, navigation and maneuver execution errors are simulated in the reduced-order model by sampling from normal distributions for the control window bounds, δe_{max} and δi_{max}, as well as the time duration of swarm maintenance.

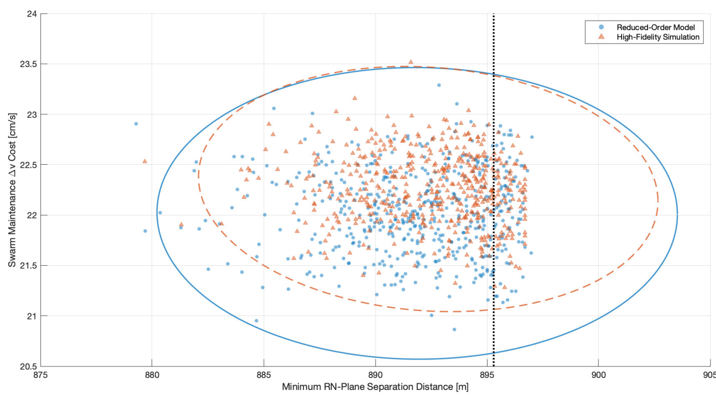

Figure 11: Swarm maintenance results.

Performing 500 runs each of the high-fidelity simulation and reduced-order model produces the distributions shown in Figure 11. The results from the reduced-order model overlap considerably with those obtained through high-fidelity simulation, with only a handful of individual simulation runs outside of the high fidelity simulation's 3-σ bounds. Each of the distributions has an abrupt cut-off at some maximum value for δr_{rn}^{min} which lies well within their 3-σ bounds. This phenomenon merits additional discussion.

The maximum value for δr_{rn}^{min} exhibited by both distributions is slightly offset from the corresponding value output by Algorithm 2 for inputs given by Eqs. 40 and 41, shown in Figure 11 as a vertical dashed line. For this scenario, that value is 895.3 m, which represents an ideal case where maneuvers are performed precisely at the control window bounds. With a controller in the loop, however, additional complications emerge. At each time step, the controller performs a check to determine if the control window bounds are being violated or if it expects that they will be violated at the next time step. In either case, a propulsive maneuver is performed in order to maintain the desired relative configuration. However, the presence of navigation errors means that these maneuvers can be performed slightly early, before the control window bounds have been reached. This results in the offset from the deterministic value from the reduced-order model, and a larger value for δr_{rn}^{min}. They can also be performed late, resulting in a smaller value for δr_{rn}^{min}. Maneuver execution errors can then have a compounding effect when an overcorrection causes the control window bounds to be further exceeded at the end of a maneuver. This results in the spread of values for δr_{rn}^{min} to the left of the vertical line. In the reduced-order model, this controller behavior is reproduced by only accepting sampled values of δe_{max} and δi_{max} which represent maneuvers executed late or, at most, a few of time steps early.

Table 7: Error statistics for swarm maintenance scenario.

	Error Mean	**Error Std Dev** (1-σ)
δr_{rn}^{min} [m]	$2.73\ (0.31\%)$	$2.15\ (0.24\%)$
Δv_{total} [cm/s]	$0.36\ (1.63\%)$	$0.26\ (1.18\%)$

As shown in Table 7, the reduced-order model produces results for Δv_{total} and δr_{rn}^{min} which are comparable to those obtained through high-fidelity simulation. Note that in the high-fidelity simulation, the path that is taken by $\delta \boldsymbol{e}$ between the maneuvers performed at u_{M_1} and u_{M_2} is neglected. During this period, the magnitude of the $\delta \boldsymbol{e}$ is briefly reduced, resulting in a smaller value for δr_{rn}^{min}. However, this effect is transient, lasting for half of one orbit, and does not negatively impact safety.

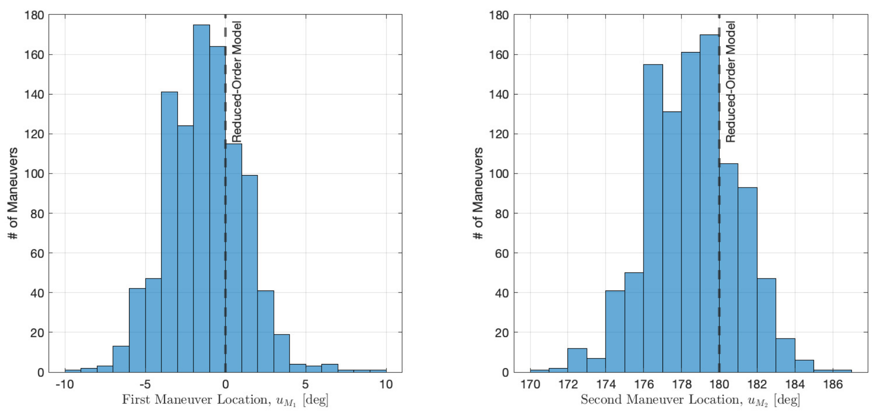

Figure 12: Swarm maintenance maneuver locations.

From Eq. 28, the reduced-order model provides in-plane maneuver locations $u_{M_1} = 0°$ and $u_{M_2} = 180°$. The distribution of values for u_{M_1} and u_{M_2} from the high-fidelity simulation are shown in Figure 12, along with the corresponding values from the reduced-order model, depicted as dashed lines. Note that there are more results to the left of the dashed line, representing maneuvers executed early. This is due to the controller behavior discussed previously.

Run-time Comparison

The need to provide reliable estimates of key mission parameters at low computational cost was a principal motivation behind the development of the reduced-order model. In order to validate that the reduced-order model is able to meet this requirement for low computational cost, its run time is compared to the run time for the high-fidelity simulation in each of the previous scenarios.

As shown in Table 8, the reduced-order model provides a speedup of more than five orders of magnitude when compared to the high-fidelity simulation. These run time tests are performed using a contemporary desktop CPU and demonstrate that the reduced-order model provides a dramatic reduction in run time compared to high-fidelity simulation, thereby enabling the rapid simulation of long-duration swarm missions.

Table 8: Simulation run times for reduced-order model and high-fidelity simulation.

Scenario	Run Time [ms]		Speedup
	High-Fidelity Simulation	Reduced-Order Model	
Swarm Reconfiguration	13604	0.11	123672
Swarm Maintenance	85457	0.15	569713

CONCLUSION

Spacecraft swarms offer significant advantages compared to monolithic spacecraft. However, these advantages come at the cost of a substantial increase in mission complexity. Mission designers working on spacecraft swarm missions must consider collision avoidance, swarm maintenance and reconfiguration, as well as the relative orbits of spacecraft within the swarm. The problem of swarm orbit design has been addressed in the literature for specific orbital scenarios, or in ways that, while more general, are complex and computationally expensive. The reduced-order model proposed in this paper provides a tool to enable the design of swarm orbits for missions lasting months or more, while providing enough flexibility for mission designers to meet diverse mission objectives.

The reduced-order model allows for the straightforward visualization of relative motion, the analytical inclusion of maneuvers and relevant perturbations, and the analytical computation of minimum inter-spacecraft separations over extended time periods. These capabilities are permitted by the parameterization of the spacecraft relative motion in terms of relative orbital elements (ROE). The reduced-order model is based on the well known method of e-/i-vector separation, a flight-proven guidance and control concept which provides passive safety for spacecraft formations. To add flexibility, swarm reconfigurations can be performed using either propulsion or differential drag.

Validation of the reduced-order model was performed through comparison with results obtained in high-fidelity numerical simulation in two scenarios representative of the challenges facing swarm missions. These results showed that the reduced-order model consistently provided accurate estimates of key mission parameters, at a significantly lower computational cost, despite the inclusion of navigation and maneuver execution errors in the high-fidelity simulation. Therefore, mission designers can utilize the reduced-order model in the design of swarm orbits with confidence that the information being provided is sufficiently accurate to inform mission design.

Currently, the reduced-order model has only been demonstrated in near-circular, low Earth orbit (LEO) scenarios. Future work should seek to improve the reduced-order model by extending it to additional orbital regimes, including eccentric orbits, orbits outside of LEO, and orbits around other central bodies. The model could also be further developed in order to output additional parameters of interest, related to scientific objectives or other mission requirements. Finally, the reduced-order model may be used in the future to efficiently generate orbit and performance data for reinforcement learning applications.

ACKNOWLEDGMENT

The authors would like to thank Celvi Lisy of the Olin College of Engineering for her assistance in providing digital renderings of the SWARM-EX spacecraft and Adam Koenig of Lockheed Martin for his assistance in proofreading mathematical derivations. This work was supported by the National Science Foundation (Award Number 1936512).

REFERENCES

[1] O. Montenbruck, M. Kirschner, S. D'Amico, and S. Bettadpur, "E/I-Vector Separation for Safe Switching of the GRACE Formation," *Aerospace Science and Technology*, Vol. 10, No. 7, 2006, pp. 628–635.

[2] E. Gill, S. D'Amico, and O. Montenbruck, "Autonomous Formation Flying for the PRISMA Mission," *Journal of Spacecraft and Rockets*, Vol. 44, No. 3, 2007, pp. 671–681.

[3] J.-S. Ardaens, S. D'Amico, and D. Fischer, "Early Flight Results from the TanDEM-X Autonomous Formation Flying System," *4th International Symposium on Spacecraft Formation Flying Missions & Technologies*, 2011.

[4] J. Sullivan, A. Koenig, J. Kruger, and S. D'Amico, "Generalized Angles-Only Navigation Architecture for Autonomous Distributed Space Systems," *Journal of Guidance, Control, and Dynamics*, Vol. 44, No. 6, 2021, pp. 1087–1105.

[5] A. Koenig, S. D'Amico, and E. G. Lightsey, "Formation Flying Orbit and Control Concept for the VISORS Mission," *AIAA Scitech 2021 Forum*, 2021.

[6] S. Lowe, M. Markevitch, and S. D'Amico, "Relative Navigation and Pointing Error Budget for an X-ray Astronomy Formation-Flying Mission," *AAS Guidance, Navigation, and Control Conference*, 2022.

[7] R. Agarwal, B. Oh, D. Fitzpatrick, A. Buynovskiy, S. Lowe, C. Lisy, A. Kriezis, B. Lan, Z. Lee, A. Thomas, B. Wallace, E. Constantino, G. Miner, J. Thayer, S. D'Amico, K. Lemmer, W. Lohmeyer, and S. Palo, "Coordinating Development of the SWARM-EX CubeSat Swarm Across Multiple Institutions," *Proceedings of the AIAA/USU Conference on Small Satellites*, 2021.

[8] R. t. Nallapu and J. Thangavelautham, "Design of Spacecraft Swarm Flybys for Planetary Moon Exploration," *AIAA Scitech 2020 Forum*, 2020.

[9] R. t. Nallapu, H. Kalita, and J. Thangavelautham, "On-Orbit Meteor Impact Monitoring Using CubeSat Swarms," *Advanced Maui Optical and Space Surveillance Technologies Conference*, 2018.

[10] L. Plice, A. D. Perez, and S. West, "HelioSwarm: Swarm Mission Design in High Altitude Orbit for Heliophysics," *AAS/AIAA Astrodynamics Specialist Conference*, 2019.

[11] A. Dono, L. Plice, J. Mueting, T. Conn, and M. Ho, "Propulsion Trade Studies for Spacecraft Swarm Mission Design," *IEEE Aerospace Conference*, 2018.

[12] A. Koenig and S. D'Amico, "Robust and Safe N-Spacecraft Swarming in Perturbed Near-Circular Orbits," *Journal of Guidance, Control, and Dynamics*, Vol. 41, No. 8, 2018, pp. 1643–1662.

[13] S. D'Amico, "Autonomous Formation Flying in Low Earth Orbit," *TU Delft*, 2010.

[14] S. Casotto, "Position and Velocity Perturbations in the Orbital Frame in Terms of Classical Element Perturbations," *Celestial Mechanics and Dynamical Astronomy*, Vol. 55, No. 3, 1991, pp. 209–221.

[15] H. Schaub, "Relative Orbit Geometry Through Classical Orbital Element Differences," *Journal of Guidance, Control, and Dynamics*, Vol. 27, No. 5, 2004, pp. 839–848.

[16] J. Sullivan and S. D'Amico, "Nonlinear Kalman Filtering for Improved Angles-Only Navigation Using Relative Orbital Elements," *Journal of Guidance, Control, and Dynamics*, Vol. 40, No. 9, 2017, pp. 2183–2200.

[17] T. Guffanti, "Optimal Passively-Safe Control of Multi-Agent Motion with Application to Distributed Space Systems," *Stanford University*, 2022.

[18] D. Brouwer, "Solution of the Problem of Artificial Satellite Theory Without Drag," *Astronomical Journal*, Vol. 64, 1959, pp. 378–397.

[19] A. Koenig, T. Guffanti, and S. D'Amico, "New State Transition Matrices for Spacecraft Relative Motion in Perturbed Orbits," *Journal of Guidance, Control, and Dynamics*, Vol. 40, No. 7, 2017, pp. 1749–1768.

[20] T. Guffanti and S. D'Amico, "Linear Models for Spacecraft Relative Motion Perturbed by Solar Radiation Pressure," *Journal of Guidance, Control, and Dynamics*, Vol. 42, No. 9, 2019, pp. 1962–1981.

[21] M. Chernick and S. D'Amico, "New Closed-Form Solutions for Optimal Impulsive Control of Spacecraft Relative Motion," *Journal of Guidance, Control, and Dynamics*, Vol. 41, No. 2, 2018, pp. 301–319.

[22] C. Foster, J. Mason, V. Vittaldev, L. Leung, V. Beukelaers, L. Stepan, and R. Zimmerman, "Constellation Phasing with Differential Drag on Planet Labs Satellites," *Journal of Spacecraft and Rockets*, Vol. 55, No. 2, 2018, pp. 473–483.

[23] V. Giralo, "Precision Navigation of Miniaturized Distributed Space Systems Using GNSS," *Stanford University*, 2021.

[24] O. Montenbruck and E. Gill, *Satellite Orbits*. Springer, 2000.

[25] O. Montenbruck and E. Gill, "State Interpolation for On-Board Navigation Systems," *Aerospace Science and Technology*, Vol. 5, No. 3, 2001, pp. 209–220.

[26] B. D. Tapley, S.Bettadpur, M. Watkins, and C. Reigber, "The Gravity Recovery and Climate Experiment: Mission Overview and Early Results," *Geophysical Research Letters*, Vol. 31, No. 9, 2004.

[27] M. Hunter and S. D'Amico, "Closed-Form Optimal Solutions for Propulsive-Differential Drag Control of Spacecraft Swarms," *AAS/AIAA Astrodynamics Specialist Conference*, 2022.

[28] D. Fitzpatrick, E. Bauch, R. Agarwal, and S. Palo, "Maximizing Mission Utility within Operational Constraints for the SWARM-EX CubeSat Mission," *AIAA SCITECH 2022 Forum*, 2022.